Available online at www.sciencedirect.com
SCIENCE DIRECT®
Journal of Membrane Science 241 (2004) 65–78
journal of MEMBRANE SCIENCE
www.elsevier.com/locate/memsci

Effect of hydrodynamics and solution ionic strength on permeate flux in cross-flow filtration: direct experimental observation of filter cake cross-sections

Volodymyr V. Tarabara [a], Ismail Koyuncu [b,c], Mark R. Wiesner [b,d,*]

[a] *Department of Civil and Environmental Engineering, Michigan State University, A136 Research Complex Engineering, East Lansing, MI 48824, USA*
[b] *Department of Civil and Environmental Engineering, Rice University, P.O. Box 1892, Houston, TX 77005-1892, USA*
[c] *Department of Environmental Engineering, Faculty of Civil Engineering, Istanbul Technical University, Maslak, Istanbul 80626, Turkey*
[d] *Department of Chemical Engineering, Rice University, P.O. Box 1892, Houston, TX 77005-1892, USA*

Received in revised form 2 April 2004; accepted 8 April 2004

Abstract

The structure of membrane cakes formed in cross-flow filtration was investigated for conditions of variable particle size and solution ionic strength. In all cases, microscopic examination of membrane cake cross-sections revealed a stratified structure: a dense region of the colloidal deposit adjacent to the membrane with an abrupt transition to a much more porous layer near the membrane–suspension interface. The thickness and structure of individual layers varied as functions of particle size and solution ionic strength. Relative specific hydraulic resistances of individual layers were estimated from regressed transport coefficients in a model describing macroscopic transport and permeate flux. This work provides direct experimental confirmation of trends predicted from theory that couples hydrodynamic conditions and interparticle interactions to describe the permeate flux performance of cross-flow filtration membranes.
© 2004 Elsevier B.V. All rights reserved.

Keywords: Ultrafiltration; Water treatment; Filter cake properties; Flux modeling; Fouling

1. Introduction

Cake formation on a membrane's surface may be an important cause of permeate flux decline [1,2]. The flux of particles to the membrane to form a cake is primarily determined by the hydrodynamics of particle transport in membrane modules. However, cross-flow hydrodynamics alone does not adequately describe observed experimental trends [3]. The structure of the cake appears to be another key parameter in determining permeate flux and must be incorporated into models describing permeate flux performance.

Cake structure has been predicted to vary as a function of particle transport and surface potential [4–7]. Moreover, this structure may be modified as a function of the relative balance between applied pressure and surface forces [8]. In the absence of restructuring, cakes formed from particles transported at lower Peclet numbers and/or from particles with higher collision efficiencies are predicted to have a more open morphology and lower hydraulic resistance [4]. Restructuring processes can further modify cake structure and resistance [9]. When the pressure across an actively forming cake achieves a critical value, the cake may collapse forming a more dense deposit. After the collapse, however, the cake porosity is expected to be largely independent of the surface chemistry of particles that form the cake. The propensity of membrane cakes for reorganization and collapse is determined by a balance of forces acting on particles in the cake. By calculating compressive pressure profiles within the filter cake and considering the effects of electrokinetic interactions between cake-forming particles, McDonogh and coworkers [10,11] have predicted cake permeability in good agreement with experimental data. Collapse of cake-forming layers near the membrane surface was predicted after a critical particle mass deposited on the membrane [12,8].

Various experimental techniques have been used to probe the porosity profile and/or overall thickness of filter cakes. Destructive methods, such as gravimetric analysis, freeze

* Corresponding author. Tel.: +1 517 432 1755; fax: +1 517 355 0250.
E-mail address: tarabara@egr.msu.edu (V.V. Tarabara).

0376-7388/$ – see front matter © 2004 Elsevier B.V. All rights reserved.
doi:10.1016/j.memsci.2004.04.030

slicing [13], cake reconstruction [14], and filter cake embedding/thin sectioning [15] have been employed to investigate cake structure. Non-destructive analyses have included small-angle neutron scattering [16], static light scattering [16], CATSCAN [17], NMR [18], laser light absorption [19], and reflection [20]. While most of these studies have yielded information on average cake structure, measurements of concentration profiles in filter cakes using the simple method of inclined filtration were recently reported [21].

The goal of this work was to investigate the effects of solution ionic strength (hence, particle surface potential) and particle size on the permeate flux and the structure of filter cakes formed in cross-flow filtration experiments. We report results of filtration experiments for nine combinations of particle size and solution ionic strength. Results of microscopic imaging of fouled membrane cross-sections are presented and correlated with the permeate flux performance for a range of experimental conditions. Further, we extend an existing macroscopic kinetic model of permeate flux and cake formation. We present analytical expressions for the transient permeate flux for membrane- and cake-limited flux cases. Through curve fitting to the derived model, indirect evidence of the coupling between effects of hydrodynamics and solution ionic strength on the permeate flux is obtained.

2. Experimental

2.1. Cross-flow membrane filtration apparatus

Experiments were performed using SEPA acrylic cross-flow flat slit membrane filtration cell (SEPA CF, Osmonics, Minneatonka, MN) in a medium-to-high foulant configuration. This bench-scale filtration apparatus is identical to that described in previous work [3]. The feed suspension was pumped over the membrane in a recycle loop using a pulse-free centrifugal pump (EC-J1, Pulsafeeder, Rochester, NY). Feed temperature was kept constant at $20\,^{\circ}\mathrm{C} \pm 0.1\,^{\circ}\mathrm{C}$. On-line spectrophotometry (Spectra 100, Spectra-Physics, San Jose, CA) was used to control the bulk concentration of particles in the suspension. Feed and permeate flow rates were measured using calibrated variable area flowmeters. Three Cole-Parmer flowmeters were connected in series at the permeate side of the module (A-03219-23 for flows up to $130.4\,\mathrm{mL\,min^{-1}}$, A-03267-18 for flows up to $46.0\,\mathrm{mL\,min^{-1}}$ and A-03219-13 for flows up to $5.5\,\mathrm{mL\,min^{-1}}$) with an air trap provided to avoid formation of air bubbles on glass floats in flowmeters. At the end of each experiment, the membrane was removed and the filtration apparatus was cleaned with detergent solution twice, and then flushed with deionized and ultrapure water, two times each.

2.2. Membranes

All experiments were performed using polysulfone membranes (NTR-7410, Hydranautics, Oceanside, CA) chemically modified to have a moderately hydrophilic surface with the contact angle measured to be 69°. Membranes with a molecular weight cutoff of 7000 Da (roughly equivalent to a pore diameter of approximately 2 nm), were chosen to eliminate the possibility of pore plugging and to selectively study the effect of cake formation on membrane fouling.

Tapping mode atomic force microscopy (AFM) imaging (NanoScope® IIIa Multi-Mode AFM™, Digital Instruments, Inc., Santa Barbara, CA) was performed to quantitatively estimate membrane surface morphology for several samples of the NTR-7410 membrane. We used etched silicon sensors (NanoWorld Pointprobe® TESP-NCH, Nanoworld AG, Neuchâtel, Switzerland) with a force constant in the range of (21 to 78) $\mathrm{N\,m^{-1}}$ and a resonance frequency in the range of (250 to 390) kHz as AFM tips. Before imaging, membranes were soaked in deionized water for 12 h and then air dried and cut to fit AFM specimen disks (Ted Pella Inc., Redding, CA). A typical AFM image is shown in Fig. 1. Values of average and root-mean-square roughness of the membrane surface calculated from the 500 nm × 500 nm scans of different locations on these membranes were (0.7 ± 0.1) nm and (0.9 ± 0.1) nm (95% confidence), respectively. The roughness is one indicator of membrane features such as pore entries. For a 10 m × 10 m scan, these values were found to be only slightly larger—2.8 nm and 2.2 nm, respectively. Comparison of these values with the size of particles used in our experiments indicates that membrane roughness was unlikely to play a significant role in determining the potential of membrane fouling by the particles.

More detailed morphological information on rough surfaces with multiple scales can be obtained by applying multifractal analysis [22,23]. Using software previously developed in our group [24], we calculated the multifractal spectrum (Fig. 2) of the membrane surface for a 10 $m \times 10$ m AFM scan. In this figure, α is Hölder exponent corresponding to the strength of the local singularity of the measure (height distribution, in this case) and $f(\alpha)$ is the fractal dimension of the subset of boxes characterized by the exponent α. In a multifractal spectrum, the broadness of the interval $[\alpha_{\min}, \alpha_{\max}]$ is indicative of the range of heights in the surface height distribution. Narrow multifractal spectrum calculated for the NTR-7410 membrane suggests that the surface morphology is regular, a result consistent with the small value of round-mean-square roughness for this surface. Another important morphological descriptor revealed by multifractal analysis is so called entropy dimension, which describes homogeneity of the spatial distribution of surface irregularities. the entropy dimension can be calculated as the value of $f(\alpha)$ for α corresponding to $f'(\alpha) = 1$. The entropy dimension calculated from AFM data is 1.99 implying that irregularities are spread evenly over the membrane surface.

In the previous work [25], we have verified that the flow in the SEPA cell in the configuration used in this work is largely unidirectional over most of the channel area with the exception of the corners of the channel. To isolate peripheral areas of the membrane and ensure ideal flow, adhesive

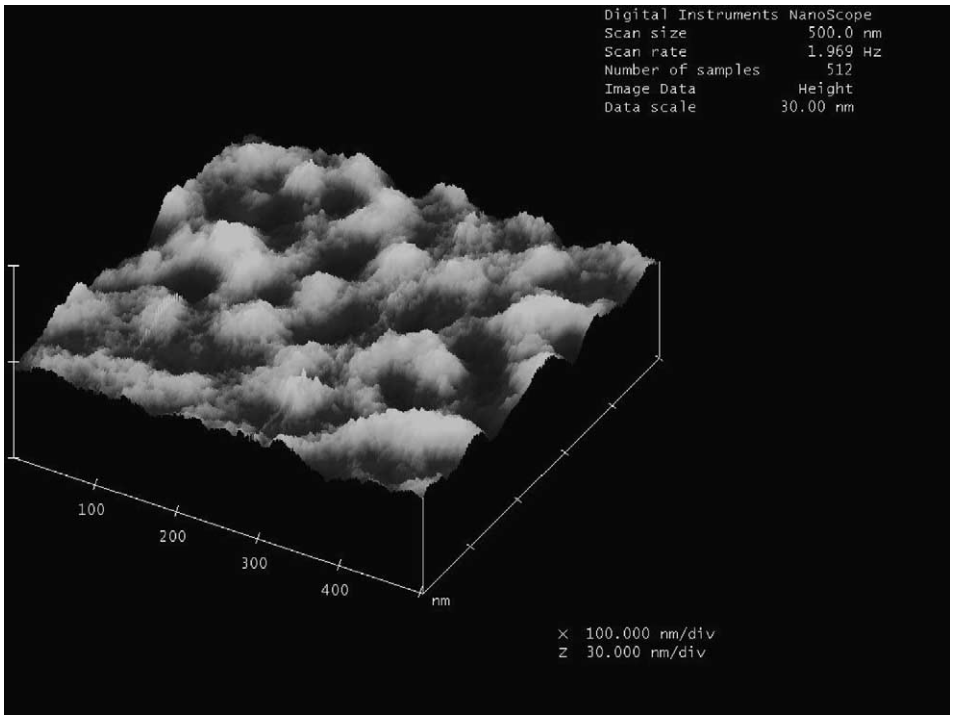

Fig. 1. Tapping mode AFM image and multifractal spectrum of the surface of NTR-7410 ultrafiltration membrane. Note that z scale is different from x and y scales.

tape was applied to the corresponding regions of the permeate side of the membrane rendering the effective area of membrane to be 21.28 cm^2.

At the beginning of each experiment, a membrane was compressed at a transmembrane pressure of 621 kPa (90 psi) until the clean water flux stabilized. The time of compression varied for different membrane samples and was in the range of (30 to 90) min. A clean water flux test was then performed to verify integrity of the membrane and to compute its hydraulic resistance. Sample-to-sample reproducibility of the initial hydraulic resistances was found to be superior to that of other types of commercial ultrafiltration membranes initially screened for this work. Nonetheless, there was an appreciable scatter in resistance values with the average membrane resistance measured to be $(1.25 \pm 0.11)\,cm^{-1}$ (see Table 1). To compensate for these differences and to ensure identical initial hydrodynamic conditions for all filtration experiments, transmembrane pressures were calculated from measured membrane resistances to yield the same initial permeate flux of $4.17 \times 10^{-3}\,cm\,s^{-1}$. The cross-flow velocity was kept constant at $11.6\,cm\,s^{-1}$. Given the hydraulic diameter of the membrane module channel (approximately 0.34 cm), the Reynolds number for the cross-flow was approximately 393, corresponding to a rapid laminar flow.

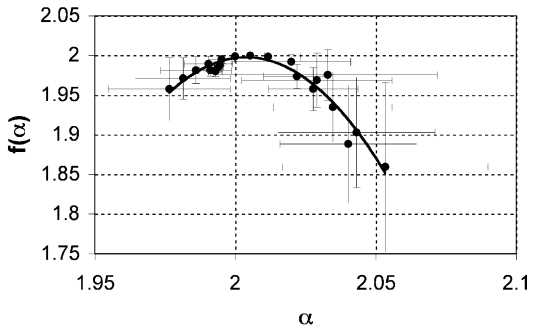

Fig. 2. Multifractal spectrum of the surface of NTR-7410 ultrafiltration membrane.

2.3. Model colloids

Spherical polystyrene particles (Bangs Laboratories Inc., Fishers, IN) of three different sizes—30 nm (lot no. 403), 110 nm (lot no. 5109), and 760 nm (lot no. 3609) were used. Manufacturer-supplied data on particle shape and size distributions of these model suspensions were verified using dynamic light scattering (DLS) and scanning electron microscopy (SEM) analyses. DLS tests (PCS 4700a, Malvern Instruments, Worcestershire, UK) were performed using 10 mm round cells for multi-angle sizing (PCS8400, Malvern Instruments). SEM images were recorded using a Phillips XL-30 FEG environmental scanning electron microscope operated in high vacuum mode.

Particles were suspended at a volume fraction of 10^{-4} in ultrapure water (Milli-Q system, Millipore Corporation, Bedford, MA) with electrical conductivity of $(0.49 \pm 0.01)\,mS\,cm^{-1}$ and ionic strength of $10^{-5}\,mol\,L^{-1}$. In other experiments, KCl was added to adjust the ionic strength to values of $10^{-3}\,mol\,L^{-1}$ or $10^{-1}\,mol\,L^{-1}$ after adjusting pH to 6.6 ± 0.05 by using $5 \times 10^{-5}\,mol\,L^{-1}$ of $NaHCO_3$.

Table 1
Experimental parameters and calculated macroscopic transport coefficients

Experiment number	I (mol L^{-1})	d_p (nm)	UV_{250}	R_m ($\times 10^{-10}$) (cm^{-1})	R_c^{ss} ($\times 10^{-10}$) (cm^{-1})	$(\hat{R}_c^{(I)}/\hat{R}_c^{(III)})$	$(\hat{R}_c^{(II)}/\hat{R}_c^{(III)})$	$k_2^{(I)}$ (min^{-1})	$k_2^{(II)}$ (min^{-1})	$k_2^{(III)}$ (min^{-1})
1	10^{-5}	30	0.032	1.40 ± 0.07	5.43	120.6	7.3	1.4×10^{-1}	4.6×10^{-2}	1.0×10^{-2}
2	10^{-5}	30	0.032	1.01 ± 0.03	5.63	117.1	7.4	1.6×10^{-1}	4.6×10^{-2}	3.9×10^{-3}
3	10^{-3}	30	0.024	0.95 ± 0.05	6.94	114.1	6.7	1.0×10^{-1}	1.3×10^{-2}	1.4×10^{-3}
4	10^{-3}	30	0.024	1.19 ± 0.07	6.77	105.3	15.9	8.0×10^{-2}	1.6×10^{-2}	3.6×10^{-3}
5	10^{-1}	30	0.032	1.33 ± 0.12	19.3	271.9	2.9	1.0×10^{-1}	1.3×10^{-2}	1.1×10^{-3}
6	10^{-1}	30	0.032	1.60 ± 0.05	16.0	225.6	4.4	1.1×10^{-1}	1.0×10^{-2}	1.3×10^{-3}
7	10^{-5}	110	0.932	1.17 ± 0.06	1.34	12.4	2.5	5.6×10^{-2}	1.3×10^{-3}	2.0×10^{-3}
8	10^{-5}	110	0.933	1.24 ± 0.04	1.21	8.2	5.8	7.1×10^{-2}	3.8×10^{-3}	2.0×10^{-3}
9	10^{-3}	110	1.320	n/a[a]	n/a[a]	6.4	5.0	4.2×10^{-2}	5.0×10^{-3}	1.9×10^{-3}
10	10^{-3}	110	0.990	1.21 ± 0.07	1.92	4.0	8.1	6.5×10^{-2}	7.7×10^{-3}	2.6×10^{-3}
11	10^{-1}	110	1.030	1.58 ± 0.03	1.29	6.0	1.6	8.6×10^{-2}	2.8×10^{-2}	5.0×10^{-2}
12	10^{-1}	110	1.020	1.30 ± 0.04	1.02	6.3	0.9	2.8×10^{-2}	1.4×10^{-2}	4.7×10^{-1}
13	10^{-5}	760	0.310	1.56 ± 0.00	1.87	47.7	2.2	4.1×10^{-1}	1.8×10^{-5}	6.3×10^{-4}
14	10^{-5}	760	0.330	1.43 ± 0.11	1.43	14.0	3.7	5.1×10^{-2}	2.0×10^{-3}	4.2×10^{-3}
15	10^{-3}	760	0.320	1.16 ± 0.06	1.62	4.2	2.7	7.7×10^{-3}	3.1×10^{-3}	1.2×10^{-3}
16	10^{-3}	760	0.370	0.87 ± 0.09	0.80	9.1	0.9	2.1×10^{-2}	1.6×10^{-3}	9.6×10^{-4}
17	10^{-1}	760	0.330	1.05 ± 0.04	0.76	9.6	n/a	2.3×10^{-2}	5.6×10^{-3}	2.9×10^{-3}
18	10^{-1}	760	0.390	n/a[a]	n/a[a]	4.2	1.1	3.2×10^{-2}	1.9×10^{-2}	5.0×10^{-2}

[a] Hydraulic resistance of clean membrane was not measured.

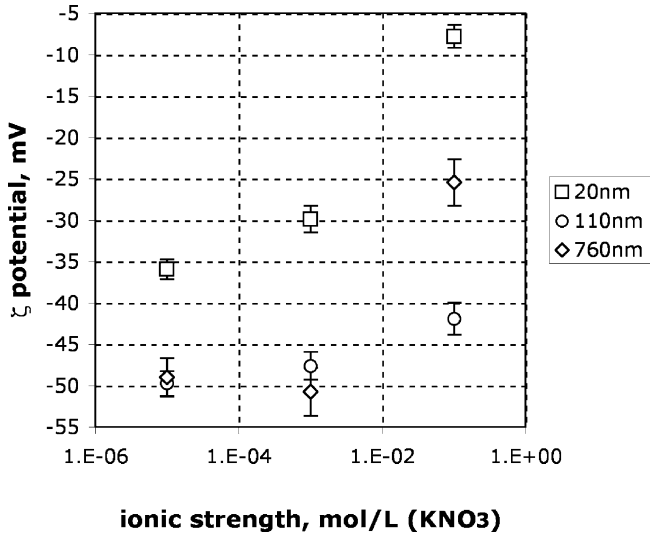

Fig. 3. Measured zeta potentials of 20 nm, 110 nm, and 760 nm polystyrene particles.

The particle aggregation state was assessed by measuring the particle size distribution in samples taken from the feed and subjected to a shear rate approximating that within the filtration cell. The Malvern granulometer (Mastersizer S, Malvern Instruments) used for that purpose has a particle size range of (0.05 to 900) m. Under the conditions imposed in these experiments, aggregation either did not occur or shear forces in the filtration cell were sufficient to break up aggregates.

Zeta-potential values for the largest (760 nm) particles were measured using Zetaphoremeter III, Model Z4000 (CAD Instruments, Les Essarts le Roi, France). For 20 nm (approximating 30 nm) and 110 nm particles, zeta potential measurements were performed using PALS Zeta Potential Analyzer (Ver. 3.25, Brookhaven Instruments Corp., Holtsville, NY). Fig. 3 summarizes results of these measurements.

2.4. Filter cake embedding and imaging

At the end of each experiment, the feed suspension was discarded, the filtration module was disassembled and cut fragments of the fouled membrane were placed into the water-miscible ultra-low viscosity embedding agent based on glycol methacrylate (“low acid” GMA, SPI-Chem, West Chester, PA). This embedding agent is often employed for the impregnation of hydrated hard-to-infiltrate biological specimens. Using a water-miscible embedding agent avoided the potential dehydration-induced damage to the filter cake structure. Filter cakes formed from the largest particles (760 nm) at the lowest ionic strength (10^{-5} mol L^{-1}) were so fragile that they disintegrated following the release of transmembrane pressure and could not be transferred to a trough with the embedding agent. For all other combinations of particle size and solution ionic

strength, there were no noticeable signs of detached or lost deposit.

Cake samples with membranes were first placed into an 85% aqueous GMA solution for 1 h and then transferred into pure GMA for overnight infiltration. At the curing stage, GMA-infiltrated samples were placed into BEEM capsules (Pelco Int.) filled with pre-polymerized GMA and were subjected to UV radiation for the period from 24 h to 72 h in PELCO UVC2 cryo chamber (Pelco Int.). It should be noted that all filter cakes, with the exception of those formed from 110 nm particles at 10^{-5} mol L^{-1} ionic strength, separated from the membrane after remaining overnight in the pure GMA. In all these cases, only separated filter cakes were transferred into capsules with pre-polymerized GMA.

After the UV curing of embedded samples was completed, blocks were cut and then doubly polished to expose filter cake cross-sections. Two thin sections per membrane (per experiment) were prepared. One thin section was imaged using polarized light microscopy both in transmitted and reflected light (Meiji 4730 light microscope, Meiji Techno Co. Ltd., Japan). Another thin section was examined with scanning electron microscopy (FEI XL30 Schottky field-emission environmental SEM/EDX in high vacuum mode). Gold was sputtered on thin section surfaces for one minute at a current of 100 mA (CRC-150 Sputtering System, TORR International Inc., New Windsor, NY) prior to the SEM imaging. SEM imaging of cakes formed from 30 nm particles was hampered by sample damage even at very low (5 kV) beam voltages. Depositing thicker Au layers to alleviate this problem was not an option as it masked the cake morphology to the extent that particles were not visible in the pseudo plane of the cross-section.

2.5. Quantification of membrane cake structure

Light microscopy and SEM images of filter cakes were analyzed using the public domain NIH Image program, version 1.62 (developed at the US National Institute of Health and available on the Internet at http://rsb.info.nih.gov/nih-image/). For each sample, calibration was performed using 21.73 m polystyrene particles (Beckman Coulter Inc., Fullerton, CA). Thickness measurements were done at locations approximately 100 m apart along the filter cake. Average values and 95% confidence intervals were calculated (Table 2).

Table 2
Calculated cake thicknesses

d_p (nm)	I (mol L^{-1})	Average total thickness (m)		Thickness (m)			
				Experiment 1		Experiment 2	
				Thin section 1	Thin section 2	Thin section 1	Thin section 2
760	10^{-5}	n/a[a]		n/a[a]			
	10^{-3}	227 ± 16	L_1	136 ± 7	149 ± 8	119 ± 6	136 ± 4
			L_2	86 ± 7	84 ± 5	91 ± 7	105 ± 4
			Total	222 ± 10	233 ± 9	210 ± 8	241 ± 6
	10^{-1}	152 ± 69	L_1	n/a[b]	106 ± 8	n/a[b]	
			L_2	n/a[b]	35 ± 3		
			Total	163 ± 16	141 ± 9		
110	10^{-5}	65 ± 18	L_1	36 ± 4	53 ± 6	n/a[b]	37 ± 3
			L_2	42 ± 5	23 ± 5	n/a[b]	25 ± 1
			Total	78 ± 6	76 ± 7	44 ± 7	62 ± 3
	10^{-3}	102 ± 73	L_1	n/a[b]	22 ± 4	n/a[b]	21 ± 3
			L_2		92 ± 7		69 ± 2
			Total		113 ± 10		90 ± 4
	10^{-1}	76 ± 7[d]	L_1	26 ± 3	n/a[b]	n/a[b]	n/a[b]
			L_2		50 ± 6	80 ± 8	139 ± 6
			Total		76 ± 7	n/a[b]	n/a[b]
30	10^{-5}	Not measurable[c]		Not measurable[c]			
	10^{-3}						
	10^{-1}						

L_1 and L_2 signify thicknesses of compressed and non-compressed layers, respectively.

[a] Filter cakes disintegrated following the release of transmembrane pressure and could not be embedded.

[b] Measurements were not done due to intermittent and/or broken cake layers.

[c] Resolution inadequate. SEM imaging at required resolution was hampered by sample damage even at very low (5 kV) beam voltages.

[d] Based on one thin section.

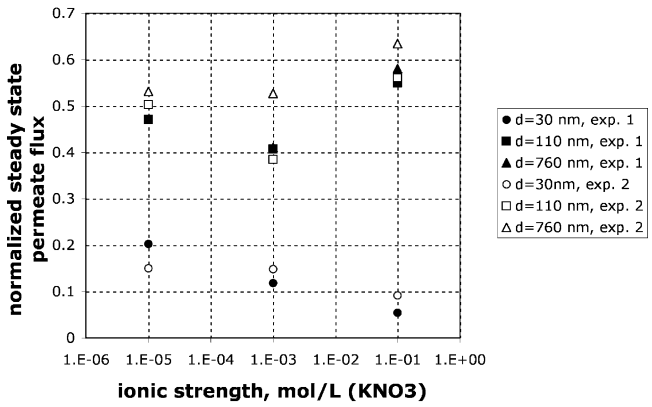

Fig. 4. Normalized steady state permeate flux as a function of particle size and ionic strength.

3. Results and discussion

3.1. Experimental results

A total of 18 cross-flow filtration experiments were conducted for three different particle sizes (30 nm, 110 nm, and 760 nm) and three ionic strengths (10^{-1} mol L^{-1}, 10^{-3} mol L^{-1}, and 10^{-5} mol L^{-1}), each combination of particle size and solution ionic strength in duplicate, for the duration of time necessary to reach the steady state permeate flux. At the end of each experiment, the membrane was embedded in water-miscible resin and then thin-sectioned.

3.1.1. Permeate flux performance

During a typical experiment, permeate flux declined and then stabilized at a steady state value. Information on permeate flux as a function of time is summarized using two parameters—the steady state permeate flux, J_{ss}, and the time to reach this flux , t_{ss} (Figs. 4 and 5).

Although steady state flux values were unambiguously calculated near the end of a filtration experiment, the determination of the time to reach steady state was subjective. Parameterization of the permeate flux curves was aided by the application of a curve-fitting procedure to models for permeate flux (see Section 3.2.3).

Steady state permeate flux passed through a minimum at the medium ionic strength for 110 nm and 760 nm particles and decreased with an increase in ionic strength for the 30 nm particles. The larger the particles, the longer it took to arrive at the steady state flux. An increase in ionic strength lead to an increase in t_{ss} values for the 30 nm particles and a steady decrease in t_{ss} values for the 110 nm and 760 nm particles. At the highest ionic strength evaluated, the time to reach steady state was approximately equal for all suspensions.

These observations can be interpreted in terms of the dependence of cake formation processes on solution chemistry and particle hydrodynamics. A lower permeate flux may be due to either a greater thickness, or higher hydraulic resistance of filter cakes, or a combination of these two factors. We propose that hydrodynamics plays a primary role in controlling the cake thickness while the hydraulic resistance of cakes is also a function of solution chemistry.

Should hydrodynamic conditions favor greater cake buildup, they will at the same time lead to a more rapid increase in the compressive pressure in the cake and will result in the collapse of the cake-forming layers adjacent to the membrane surface. The condition for the collapse is given by a balance of forces acting on particles in the cake. This balance strongly depends on the solution chemistry as factors such as solution ionic strength determine the degree of electrostatic repulsion between particles. Due to thinner Debye layers surrounding particles and weaker interparticle repulsion, filter cakes formed at higher ionic strengths are

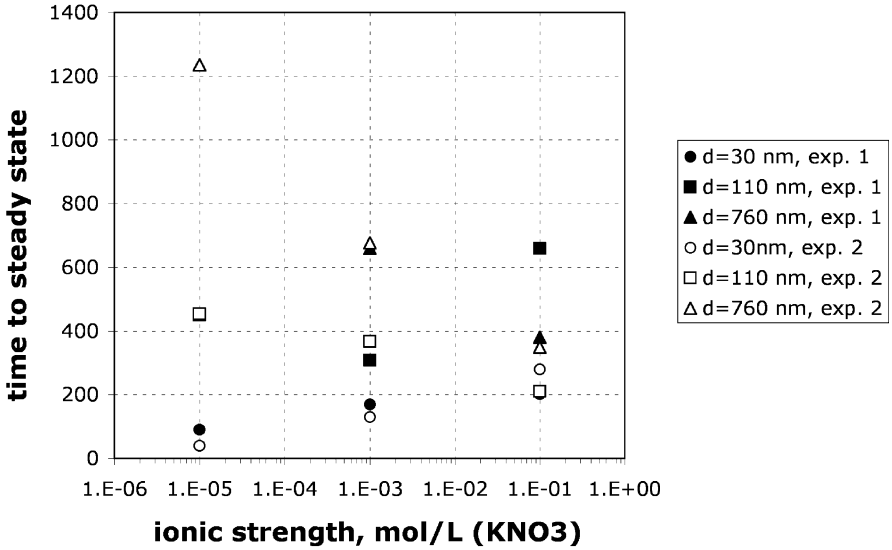

Fig. 5. Time to reach the steady state as a function of particle size and ionic strength.

anticipated to collapse at lower compressive pressures. A collapsed layer will a have higher hydraulic resistance and, under conditions of constant transmembrane pressure, will lead to a decrease in permeate flux. A lower permeate flux corresponds to a decrease in particle flux to the cake and a slower cake buildup. Thus, the portion of the cake deposited at the reduced flux will have a looser, more porous morphology, a lower hydraulic resistance, and will be more prone to reorganization, collapse, or both. This more porous layer will grow until its total thickness is large enough to produce a compressive pressure that results in the collapse of the portion of the loose layer adjacent to the membrane or a previously collapsed layer. This process is expected to continue until cake thickness is great enough such that shear forces prevent further deposition. Thus, such a process should yield cakes consisting of two layers—one compact (collapsed) and one loose layer—formed as a result of multiple growth-collapse cycles. Total thickness as well as thicknesses of compact and loose layers are determined by flow hydrodynamics and particle surface potentials. Particle transport models coupled with calculations of interparticle forces must be used to calculate these thicknesses for each combination of particle size and surface potential.

3.1.2. Structure and specific hydraulic resistance of filter cakes

The most striking feature of the filter cakes observed by light and electron imagery was that of stratification. Very dense regions of the cakes were observed adjacent to the membrane. These dense regions rapidly transitioned to a much more porous layer (Figs. 6–10). The two-layer structure of filter cakes could be easily identified in polarized and non-polarized transmitted light for all combinations of ionic strength and particle size for which thin sections were prepared. Darker color in the images corresponds to higher porosity.

Fig. 6 illustrates a filter cake on a composite membrane consisting of three support layers and a very thin skin layer (not visible in the figure). An upper layer of the filter cake can be seen to peel off from the lower layer. This cake was formed from particles 110 nm in size and at 10^{-5} mol L^{-1} ionic strength. All other images depict only filter cakes because membranes detached from filter cakes during the embedding process as described in Section 2.4. Figs. 7 and 8 depict filter cakes formed from 110 nm particles at 10^{-3} mol L^{-1} and 10^{-1} mol L^{-1} ionic strength, respectively. In Fig. 7, the darker region in the middle of the filter cake is an empty space separating the denser and looser layers. Similar results were obtained at all ionic strengths. However, the optical contrast in different filter cakes is not the same. The higher the ionic strength at which the cake was formed, the more pronounced was the difference in optical properties of distinct layers in the cake. Higher ionic strengths are anticipated to produce deposited layers that are more porous before collapse, but also most susceptible to collapse. After such a deposit collapses, however, the resulting structure is expected to be more dense and to be similar to that of collapsed layers formed from particles with lower collision efficiency at lower ionic strengths.

Figs. 9 and 10 show filter cakes formed from 760 nm particles at 10^{-3} mol L^{-1} and 10^{-1} mol L^{-1} ionic strength, respectively. The two-layer structure was obvious for the case of 10^{-3} mol L^{-1} ionic strength (Fig. 9). That is, both, collapsed and non-collapsed layers were present in the cake. At higher magnification, a gradual change in porosity within individual layers of the cake formed from 760 nm particles at 10^{-3} mol L^{-1} ionic strength is apparent (Fig. 11). The history of cake collapse is evident in the decreased porosity moving away from the membrane. This SEM image shows both the porosity gradient and sharp borders between layers interpreted as evidence of collapse and/or reorganization events during cake growth. Such step-wise porosity profiles were predicted in recent theoretical works [8,12].

Cakes formed from 760 nm particles at 10^{-5} mol L^{-1} ionic strength were too fragile to prepare thin sections and, therefore, corresponding filter cake images are not avail-

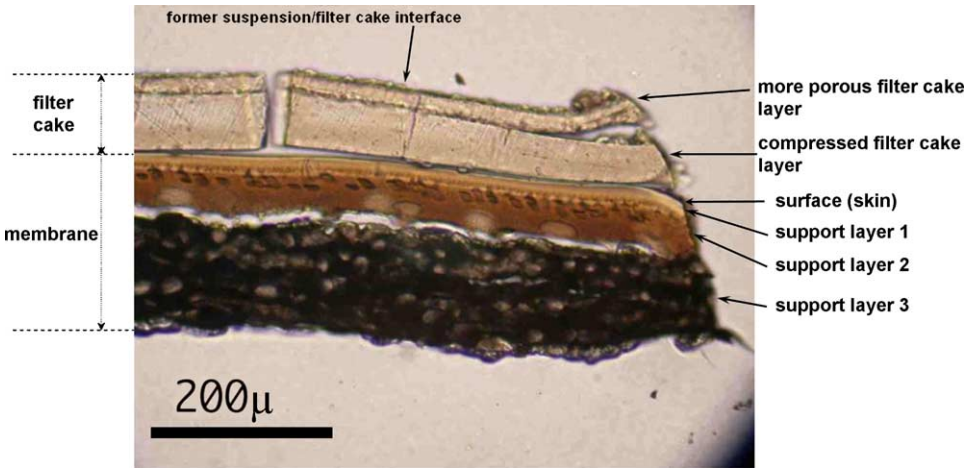

Fig. 6. Filter cake cross-section imaged in transmitted light, $d_p = 110$ nm, $I = 10^{-5}$ mol L^{-1}.

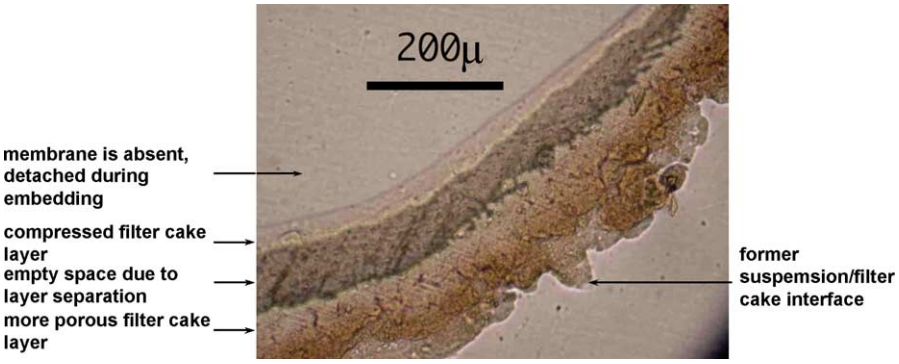

Fig. 7. Filter cake cross-section imaged in transmitted light, $d_p = 110\,\text{nm}$, $I = 10^{-3}\,\text{mol}\,\text{L}^{-1}$.

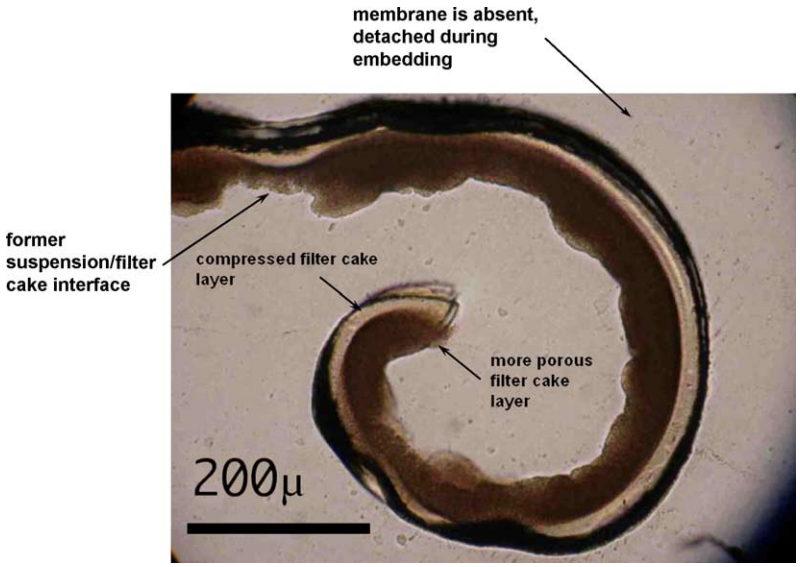

Fig. 8. Filter cake cross-section imaged in transmitted light, $d_p = 110\,\text{nm}$, $I = 10^{-1}\,\text{mol}\,\text{L}^{-1}$.

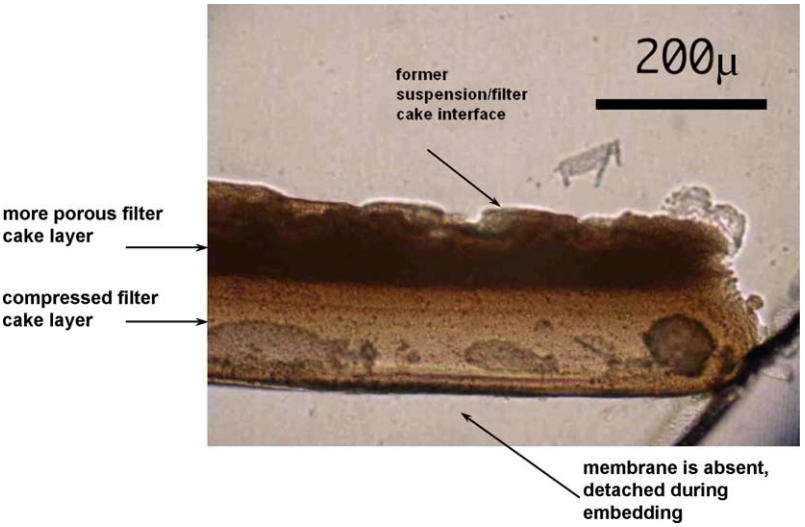

Fig. 9. Filter cake cross-section imaged in transmitted light, $d_p = 760\,\text{nm}$, $I = 10^{-3}\,\text{mol}\,\text{L}^{-1}$.

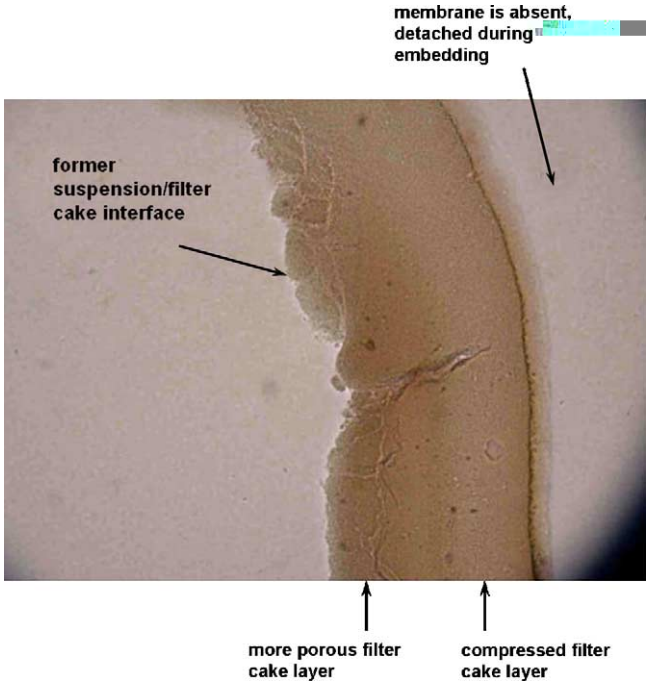

Fig. 10. Filter cake cross-section imaged in transmitted light, $d_p = 760$ nm, $I = 10^{-1}$ mol L^{-1}.

able. In the case of membranes fouled by 30 nm particles, thin sections were prepared, but cakes were not discernible on the membrane surface. SEM imaging at required resolution was hampered by sample damage even at very low (5 kV) beam voltages. The measured thickness of the cross-sections was not found to be statistically different from that of the clean membranes. It appears that due to the very high specific resistance of filter cakes formed from 30 nm particles, the deposition of even very thin particle layers was sufficient to produce a 90% flux decline.

The thicknesses of individual layers were measured for all available filter cake images (Table 2). Generally, cake thickness can not be used as a single predictor of the cake resistance because filter cakes formed at different ionic strengths are expected to have different specific resistances. However, specific resistances of collapsed filter cakes composed of particles of the same size may be expected to be similar. For a homogeneous cake of constant porosity, the hydraulic specific resistance, $\hat{R}_c$, of the cake can be estimated using the Kozeny–Carman equation [26,27]:

$$\hat{R}_c = \frac{180(1-\epsilon)^2}{d_p^2 \epsilon^3} \quad (1)$$

where d_p is the particle size and ϵ is the porosity of the particle deposit.

Fig. 11. SEM image of the cross-section of the filter cake formed from 760 nm polystyrene particles at 10^{-3} mol L^{-1} ionic strength.